Suzaku Observation of Diffuse X-ray Emission from the Carina Nebula

Kenji HAMAGUCHI[1,2], Robert PETRE[1], Hironori MATSUMOTO[3], Masahiro TSUJIMOTO[4], Stephan S. HOLT[5], Yuichiro EZOE[6], Hideki OZAWA[7], Yohko TSUBOI[8], Yang SOONG[1,2], Shunji KITAMOTO[4], Akiko SEKIGUCHI[4], Motohide KOKUBUN[9]

[1]*Exploration of the Universe Division, NASA Goddard Space Flight Center, Greenbelt, MD 20771, USA*

[2]*Universities Space Research Association, 10211 Wincopin Circle, Suite 500, Columbia, MD 21044-3432, USA*

[3]*Department of Physics, Graduate School of Science, Kyoto University, Kita-Shirakawa, Sakyo-ku, Kyoto 606-8502*

[4]*Department of Physics, Faculty of Science, Rikkyo University, 3-34-1 Nishi-Ikebukuro, Toshima-ku, Tokyo 171-8501*

[5]*Franklin W. Olin College of Engineering, Needham, MA 02492, USA*

[6]*The Institute of Space and Astronautical Science, 3-1-1 Yoshinodai, Sagamihara, Kanagawa 229-8510*

[7]*Graduate School of Science Earth and Space Science Osaka University, Machikaneyama 1-1, Toyonaka Osaka, 560-0043*

[8]*Department of Physics, Faculty of Science and Engineering, Chuo University, 1-13-27 Kasuga, Bunkyo-ku, Tokyo 112-8551*

[9]*Department of Physics, University of Tokyo, 7-3-1 Hongo, Bunkyo-ku, Tokyo 113-0011*

kenji@milkyway.gsfc.nasa.gov

(Received ; accepted)

Abstract

We studied extended X-ray emission from the Carina Nebula taken with the *Suzaku* CCD camera XIS on 2005 Aug. 29. The X-ray morphology, plasma temperature and absorption to the plasma are consistent with the earlier *Einstein* results. The *Suzaku* spectra newly revealed emission lines from various spices including oxygen, but not from nitrogen. This result restricts the N/O ratio significantly low, compared with evolved massive stellar winds, suggesting that the diffuse emission is originated in an old supernova remnant or a super shell produced by multiple supernova remnants. The X-ray spectra from the north and south of η Car showed distinct differences between 0.3−2 keV. The south spectrum shows strong L-shell lines of iron ions and K-shell lines of silicon ions, while the north spectrum shows them weak in

intensity. This means that silicon and iron abundances are a factor of 2–4 higher in the south region than in the north region. The abundance variation may be produced by an SNR ejecta, or relate to the dust formation around the star forming core.

Key words: ISM: abundances — ISM: individual (Carina nebula) — supernova remnants — X-rays: ISM

1. Introduction

Not a few giant H II regions emit extended soft X-rays with kT ~0.1–0.8 keV, log $L_{\rm X}$ ~33–35 ergs s^{-1}, and extent ~1–10^3 pc (RCW38: Wolk et al. 2002, M17: Townsley et al. 2003, NGC6334: Ezoe et al. 2006, Carinae Nebula: Seward et al. 1979; Seward & Chlebowski 1982; Evans et al. 2003, extragalactic H II regions: Kuntz et al. 2003, Strickland et al. 2004). This high surface brightness cannot be accounted for by an extrapolation of the discrete source luminosity function, and thus is thought to arise from diffuse plasma. The required plasma temperature and thermal energy can be produced by collisions or termination of fast winds from main-sequence or embedded young O stars (Seward & Chlebowski 1982; Townsley et al. 2003; Ezoe et al. 2006), but the extended emission is often observed from regions apart from massive stellar clusters. Another origin, such as an unrecognized supernova remnant (SNR), cannot be ruled out.

In principle, the origin of the diffuse emission can be determined by measuring its composition. For example, the plasma should be overabundant in nitrogen and neon if it originates from winds from a nitrogen-rich Wolf-Rayet star (WN), while it would be overabundant in oxygen if it arises from a Type II SNR. The temperature of the plasma, typically a few million degrees, make soft X-ray band studies highly desirable, because of the presence in this band of strong lines from these elements, plus carbon, silicon and iron.

The Carina Nebula, which contains several evolved and main-sequence massive stars such as η Car, WR 25 and massive stellar clusters such as Trumpler 14 (Tr 14), emits soft diffuse X-rays 10–100 times stronger than any other Galactic giant H II region ($L_{\rm X}$ ~10^{35} ergs s^{-1}, Seward et al. 1979). The high surface brightness made possible the discovery of the diffuse emission by the *Einstein* Observatory in the late 1970's. The *Einstein* observations revealed that the diffuse emission tends to be associated with optically bright regions containing massive stars, and is strongest in regions bordering the western part of the V-shaped dust lane (Seward & Chlebowski 1982). Recent *Chandra* observations provided a point source free measurement of the diffuse flux (Evans et al. 2003), and suggested high elemental abundances of O, Ne, Si and Fe to be more than ~2 solar (Townsley et al. 2005).

No detailed abundance measurement of the diffuse emission from the Carina Nebula has been made. The X-ray CCD cameras (XISs: X-ray Imaging Spectrometer) onboard the

Suzaku observatory have the best spectral resolution for extended soft X-ray emission. It is thus suitable for measuring the abundance of key elements in the diffuse plasma. To compensate for the limited angular resolution of *Suzaku*, we have also utilized the archival *XMM-Newton* (Jansen et al. 2001) and *Chandra* (Weisskopf et al. 2002) data from the Carina Nebula to investigate the spatial distribution of the diffuse emission and the contamination from X-ray point sources.

2. Observations & Data Reduction

Suzaku (a.k.a. Astro-E2, Mitsuda et al. 2006) is the 5th Japanese X-ray observatory, developed by a Japanese-US collaboration, and successfully launched on 2005 July 10. The observatory has five X-Ray Telescopes (XRT, Serlemitsos et al. 2006) with four CCD focal plane detectors (XIS, Koyama et al. 2006) and an X-ray calorimeter (XRS, Kelly et al. 2006), which unfortunately malfunctioned a month after the launch. The observatory also has a hard X-ray detector (HXD, Takahashi et al. 2006; Kokubun et al. 2006). The XIS comprises four CCD cameras, XIS0 through XIS3, three of which (XIS 0, 2 and 3) use front-illuminated (FI) CCD chips while XIS1 utilizes the back-illuminated (BI) technology. Compared with CCD detectors on earlier X-ray observatories, both the BI and FI chips have better spectral resolution at energies below $\sim$1 keV: their FWHM energy resolution at 0.5 keV is $\sim$40 eV (FI) and $\sim$50 eV (BI), with negligible low-energy tails.

Suzaku observed the Carina Nebula twice, on 2005 Aug. 29 and 2006 Feb. 3, with similar pointings, putting η Car at the center of the XIS FOV (Figure 1). In both observations, the XISs were operated with the Normal mode. The first observation was 16 days after the XIS first light (2005 Aug 13) when contamination on the optical blocking filter was almost negligible, while the second observation, 174 days after the first light, suffered significant degradation of the soft response by progressive contamination on the XIS of a factor of $\sim$2 between 0.4–0.5 keV on axis. We thus did not analyze the second observation in this paper. We also did not use the HXD data, whose X-ray signals are mostly from η Car.

For the version 0.7[1] unscreened data, we screened out hot and flickering pixels with `cleansis` and removed exposure frames with telemetry saturation. We excluded the data taken during the South Atlantic Anomaly (SAA) passage and within 256 sec after the passage. We then selected data taken during cut-off-rigidity (COR) above 4 GeV, elevation from the Earth (ELV) above 5° and elevation from the sun-lit Earth rim (DaY Earth ELeVation:

[1] The version 0.x process uses the earliest detector calibration and *Suzaku* software still under development, and was released only to the Suzaku team members (Science Working Group: SWG) to verify the data quality. The process does not perform some detailed calibration of the data, such as correction of the satellite wobbling and event time tagging optimized for the XIS operational mode. The latest processing as of 2006 July is version 0.7, which achieved an absolute energy scale within $\pm$5 eV below 1 keV and $\pm$0.2% at the iron Kα energy for the XIS data.

DYE_ELV) above 10° for the FI data and 20° for the BI. The tight DYE_ELV filtering criterion for the BI was to minimize contamination of neutral nitrogen and oxygen lines from the day Earth atmosphere. There were no remarkable particle background flares that degraded the data quality. The net exposure of the each FI chip and the BI were ~60 ksec and 49.0 ksec, respectively. We used the HEAsoft[2] analysis package ver. 6.0.6 for data analysis. In spectral fits, we used the XIS response matrices released on 2006-02-13 and generated auxiliary files with `xissimarfgen-2006-05-28`, which considers additional absorption due to the XIS contamination.

3. Spatial Distribution of the X-ray Sources

To understand the spatial distribution of the diffuse X-ray emission and X-ray point sources in the field, we surveyed archival *XMM-Newton* data-sets aimed at η Car. There are in total 11 observations performed between 2000 and 2003[3]. Figure 1 shows a true color image accumulated from all the MOS data taken with the prime full window mode (*red*: 0.2–0.6 keV, *green*: 0.6–1.2 keV, *blue*: 1.2–10 keV). The image depicts several bright X-ray point sources: η Car (LBV star), WR25 (Wolf-Rayet star), HD 93250 and HD 93205 (O3 stars), and Tr 14 (massive stellar cluster), as well as multiple weak point sources especially concentrated between η Car and WR 25. The image also clearly shows two kinds of apparently extended emission, seen as red and green. The "red" emission — relatively strong below 0.6 keV — is located between Tr 14, WR 25 and η Car. As is suggested by Seward & Chlebowski (1982), the emission is stronger at the west side with a sharp cut-off at the boundary of the V-shaped optical dark lane. The "green" emission — relatively strong above 0.6 keV — is located to the south of η Car, extending east-west, where another optical dark lane and CO gas condensation are located (Yonekura et al. 2005, also see Figure 1).

The *Suzaku* XIS FOV (Figure 1) covers most of the X-ray point and extended sources detected in the *XMM-Newton* image. Among the point sources, the XIS image resolves four bright X-ray sources, η Car, WR 25, HD 93250 and HD 93205. To minimize contamination, we excluded regions around these sources, within $4'$ from η Car and $2'$ from the other three sources. We then defined the "north" and "south" regions as in Figure 1, to extract spectra of the "red" and "green" emission, respectively. We excluded an area between the north and south regions containing multiple weak point sources. Bright spots on the BI image at the upper and lower right corners are ^{55}Fe calibration sources. We included these regions in the BI data to increase the photon statistics for the diffuse emission, since the calibration sources do not significantly contaminate the spectrum outside 5.9 and 6.4 keV, while we removed them from the FI data so we could investigate the Fe K line profile around 6–7 keV.

[2] http://heasarc.gsfc.nasa.gov/docs/software/lheasoft/

[3] Sequence ID: 112580601, 112580701, 145740101, 145740201, 145740301, 145740401, 145740501, 160160101, 160160901, 145780101, 160560101, 160560201, 160560301.

4. Characteristics of the North and South Spectra

We extracted all the XIS0-3 spectra from both the north and south regions and combined the spectra of the FI chips (XIS0, XIS2 and XIS3), whose spectral responses are almost identical. (Hereafter, we call the combined spectrum as "FI spectrum".) We overlaid these FI and BI spectra of the north and south regions on spectra accumulated from observations of the night side of the Earth (Figure 2). Events detected during the night Earth observations originate from particle background, X-ray fluorescence of Ni, Au and Si inside the camera body, ^{55}Fe calibration source and detector electronic noise. To reproduce the background of the Carina Nebula spectra correctly, we extracted each night Earth spectrum from the region corresponding to the source region on the detector map and weighted the spectrum for exposures at each COR value during the observation. The night Earth spectra match with the observed spectra at $\gtrsim$10 keV for the FI with less than $\sim$7.5% discrepancy, and $\gtrsim$8 keV for the BI with less than $\sim$2.5% discrepancy. A small discrepancy by $\sim$10% is seen in lines from the ^{55}Fe calibration source, which decayed from the Carina Nebula observation on 2006 Aug 29 to the span between 2005 September – 2006 May when the night Earth spectra were accumulated. This means that the internal background during this observation is well reproduced with the night Earth spectra, and we therefore use the night Earth data as a background in subsequent analysis. Both the north and south spectra show substantial excess X-ray emission above the background level between 0.2–10 keV, including prominent emission lines.

The north and south spectra show similar spectral features above 2 keV and below 0.3 keV. Above 2 keV, both spectra show emission lines from S XV, S XVI, Ar XVII and Fe XXV ions, emitted from hot plasma with $kT \gtrsim 2$ keV, as well as a marginal detection of fluorescence from cold iron at 6.4 keV. The south region has $\sim$60–70% of the number of events from the north region, which just corresponds to the ratio of the effective area, and does not strongly depend on the photon energy. This means that the flux level and continuum slope are also similar between the north and south spectra above 2 keV. This similarity is seen for emission below 0.3 keV as well, though it is only measurable with the BI. The north and south spectra show no remarkable variation below 0.3 keV and above 2 keV.

In contrast, the spectra between 0.3–2 keV are conspicuously different. Figure 3 shows an overlay of the BI spectra between 0.3–2 keV, with the north spectrum normalized by 64% to compensate for the effective area difference at 2 keV. A strong difference is seen between 0.7 keV and 1.2 keV, which apparently is the source of the two colors of diffuse emission in Figure 1. The band in which the difference is found is dominated by emission lines from the iron L-shell complex. Additionally, the south spectrum shows a stronger Si XIII line and possibly a stronger C VI line at $\sim$0.39 keV, while the north spectrum shows a clear excess at and below the O VII line. The south spectrum shows no clear evidence of lines from Ne IX or Ne X ions, but these could be hidden by the Fe L-shell complex. Except for the energy bands with these

emission lines, the spectral shapes look similar. This suggests that the differences represent an elemental abundance variation, and not a temperature difference. We should note that though a small marginal peak at 0.5 keV looks like an emission line of hydrogen-like nitrogen, it is more likely produced by a combination of interstellar absorption and the instrumental oxygen edge at 0.54 keV.

These results suggest that the spectra from both regions are roughly divided into three components: emission above 2 keV (hard component, hereafter HC) and below 0.3 keV (soft component, SC), which do not differ significantly between the north and south regions; and emission between 0.3 and 2 keV (medium component, MC) with remarkable variation in some emission lines. We see strong variation in emission lines from the Fe L-shell complex in the MC, but not even slightly in emission lines from Fe XXV ions in the HC. This supports the idea that each component has a different origin.

5. Contamination from X-ray Sources

Both spectra include emission from numerous point sources that are not resolved with *Suzaku* (see the *XMM-Newton* image in Figure 1), Cosmic X-ray Background (CXB) radiation, Galactic Ridge X-ray Emission (GRXE) and Local Hot Bubble (LHB) emission. In this section, we estimate the contribution of these contaminants in the *Suzaku* spectra. We plot their estimated contribution in Figure 4, using point or extended source responses generated with `xissimarfgen-2006-05-28`.

5.1. Point Sources

In a *Chandra* observation in 1999, Evans et al. (2003) detected 25 and 12 X-ray point sources from the north and south regions, respectively. They estimated the X-ray flux of each detected source from its count rate, assuming a typical stellar spectrum and extinction to the Carina Nebula ($\log T = 6.65$ K, $N_{\rm H} = 3{\times}10^{21}$ cm^{-2}). However, several point sources in the field are found to have significantly higher plasma temperature than the typical stellar coronal source (Albacete Colombo et al. 2003; Evans et al. 2004). This means that representing the contribution of unresolved point sources in the *Suzaku* spectra using a typical stellar spectrum scaled to the total point source flux calculated from tables in Evans et al. (2003) would be incorrect. We therefore analyzed the archival *Chandra* observation of the Carina Nebula.

The *Chandra* observation we analyzed was performed with the ACIS-I detector on 1999 Sep. 6 for 21.5 ksec (sequence ID: 50, 1249), and has about twice the exposure of the data set used in Evans et al. (2003). In this observation, the ACIS-I covered most of the XIS FOV (see Figure 1).

We extracted X-ray events of each point source in Evans et al. (2003) from an encircled region that includes 90% of the point source emission. Background is taken from a nearby source free region, though it is almost negligible. Figure 5 depicts the composite spectra of the

point sources in the north and south regions. The south spectrum appears featureless, while the north spectrum shows weak neon and magnesium features. Each spectrum was fitted using an absorbed 2-temperature (2T) model (WABS, Morrison & McCammon 1983; the APEC[4] code, Table 1). We added a Gaussian component at $\sim$1 keV for the north spectrum to reproduce an apparent excess from a neon line that remained in the 2T fit. Models of both spectra are reproduced at slightly less than 90% confidence, possibly because of marginal line features around 1 keV and 1–3 keV. Both best-fit models have high kT $\sim$2–4 keV and consistent $N_{\rm H}$ values with the interstellar absorption to the Carina Nebula. The extremely low abundances are artifacts of combining spectra from multiple sources. The point source contribution to the *Suzaku* to the north and south regions is less than $\sim$25 % of the total flux.

5.2. CXB, GRXE, LHB and η Car

For a CXB spectrum we use model Id1 in Table 2 of Miyaji et al. (1998), which suggests a CXB flux fluctuation between regions of $\lesssim$30%. We assumed $N_{\rm H}$ at 1.3×10^{22} cm^{-2}, the Galactic H I column density to the Carina Nebula (Dickey & Lockman 1990). The CXB flux contribution to the north and south spectra is $\lesssim$10%.

To estimate the GRXE flux around the Carina Nebula (l, b) $\sim$(287.°60, $-$0.°63) we referred to a 3–20 keV Galactic plane map taken with Rossi X-ray Timing Explorer (RXTE) (see the top panel of Figure 7 in Revnivtsev et al. 2006). In this map, the Carina Nebula is heavily contaminated by emission from η Car because of the limited RXTE spatial resolution. We therefore measured X-ray flux at slightly higher (l $\sim$290°) and lower (l $\sim$285°) Galactic longitudes along the Galactic plane, where bright X-ray point sources are apparently absent, and interpolated those values to infer a GRXE flux at the Carina Nebula of $\sim1.4\times10^{-11}$ ergs cm^{-2} s^{-1} deg^{-2} (3–20 keV). We assumed the GRXE spectral shape measured by Ebisawa et al. (2005) at (l, b) $\sim$(28.°5, 0.°0) and reduced the normalization by a factor of 5 to match the GRXE flux at the Carina Nebula. The GRXE emission contributes approximately the same flux as the CXB between 1 and 8 keV, $\lesssim$10% of the total.

Emission from LHB toward the Carina Nebula has an insignificant spatial variation over degrees, and has a surface brightness of $\sim4\times10^4$ counts s^{-1} arcmin^{-2} in the ROSAT PSPC R1+R2 band (Snowden et al. 1998). Assuming a Raymond-Smith thin-thermal plasma model (Raymond & Smith 1977), the LHB emission with kT $\sim$0.1 keV accounts for $\sim$30% of the 0.2–0.3 keV flux. We should note that the Raymond-Smith and APEC models have a factor of 3 discrepancy in flux at kT $\sim$0.1 keV, due to calculated line strength differences. Since emission from the Carina Nebula should be cut off around $\sim$0.4 keV by interstellar absorption, the residual emission below 0.4 keV probably also arises in the foreground.

Emission from the star η Car is an order of magnitude stronger than any other source in the field and thus can contaminate a substantial fraction of the XIS FOV. We reproduced

[4] http://cxc.harvard.edu/atomdb/sources_apec.html

the η Carspectrum from the same *Suzaku* data using an empirical model and estimated that the contamination is almost negligible for the south region and $\lesssim$10% for the north region.

5.3. Total Contribution

Figure 4 depicts the total contribution of potential contaminants to the *Suzaku* spectra. Between $\sim$0.3 and 2 keV, the contamination should be negligible, $\lesssim$10 % in both the north and the south spectra. Above $\sim$2 keV, the contamination accounts for $\sim$30–40% of the total X-ray flux. Below 0.3 keV, the LHB accounts for $\sim$30% of the observed flux.

The point source flux estimate has several uncertainties. First, several marginal sources appear in the *Chandra* image that are not catalogued in Evans et al. (2003). An eyeball estimate indicates that these sources contribute as much as an additional $\sim$40% in photon flux of the detected point sources. Second, the ACIS-I FOV does not cover $\sim$15% of the north region and $\sim$37% of the south region. However, in the *XMM-Newton* image, there are only a few point sources in the uncovered portion of the north missing region and none in the south. Third, variability of point sources must be taken into account, though we do not expect sources to vary in concert. From these considerations, we estimate that point sources can contribute as much as 1.5–2 times the flux given in §5.1.

In combination, the contamination sources contribute up to half of the *Suzaku* flux above 2 keV. This, in turn, means that half of the hard band flux cannot be attributed to contaminants. On the other hand, the excess between 0.3 and 2 keV is a factor of 3–10 higher than the total of possible contaminants and therefore originates in diffuse plasma.

6. Spectral Fits

To quantitatively estimate the spectral parameters of the diffuse emission, we simultaneously fitted the FI and BI spectra above 0.3 keV for each region. We tentatively assumed an absorbed 1T thin-thermal plasma (WABS, Morrison & McCammon 1983; APEC code) for the HC, which should really originate from multiple emission components as seen in §5. For the MC, we first assumed an absorbed 1T thin-thermal plasma, which however failed to reproduce both the spectral slope above 1 keV and the strong emission line from O VII ions. We therefore assumed a commonly absorbed 2T thin-thermal plasma (MC_{cool} and MC_{hot}). We omitted data below 0.3 keV, that is the SC, and BI data points between 5.5–6.7 keV, where emission from ^{55}Fe calibration source dominates. We separately varied elemental abundances between the HC and MC. We also individually varied the abundance of each element of the MC, but tied the abundances of the same elements between MC_{cool} and MC_{hot}.

Calibration uncertainty is still a concern at the time of writing this paper. To adjust the effective area between the XIS sensors we varied the BI normalization by multiplying an energy independent coefficient to the BI model ("constant" model in `xspec`). To allow for uncertainty in the absolute energy scale of each spectrum we allowed the gain to vary ("gain fit" function

in xspec). In the best-fit models, the BI spectra of the north and south regions have ~11% and ~5% higher normalization than the FI spectra, respectively. Other *Suzaku* observations also show ~3% normalization inconsistency between the BI and FI (e.g., NGC 2110, Bamba et al., private communication). A remaining ~5% discrepancy in the north spectra is perhaps caused by removing the north-west corner of the XIS0 and XIS3 data to exclude ^{55}Fe calibration sources, where diffuse emission is relatively strong. The slope and offset of the energy scale settled around ~2.1% and 12 eV for the BI south spectrum and ~0.1−0.4% and ~1−7 eV for the others, values generally consistent with other rev 0.7 data. In subsequent fits, we fixed these parameters at their best-fit values.

The best-fit models (Table 2) reproduce neither of the spectra with a goodness of fit acceptable above 90% confidence. This might be caused by poor calibration and/or inaccuracy in the emission line code, which we describe in detail later. In this model, plasma temperatures of both spectra are similar to each other, but the north spectrum has an order of magnitude larger cool component emission measure $E.M.(\mathrm{MC}_{cool})$ and a factor of two larger $N_{\mathrm{H}}(\mathrm{MC})$ than the south spectrum. A factor of 2 larger N_{H} value for the north region seems inconsistent with a thick CO condensation being around the south region (Yonekura et al. 2005), though we do not know locations of the X-ray plasma and the CO condensation along the line of sight. Moreover, it would be too convenient to think that the north region happens to have an order of magnitude larger $E.M.(\mathrm{MC}_{cool})$, and, as a result, have a 0.3−0.5 keV observed flux similar to the south region. Since $E.M.(\mathrm{MC}_{cool})$ and $N_{\mathrm{H}}(\mathrm{MC})$ can easily couple in a spectral fit, it is possible that the differences of $E.M.(\mathrm{MC}_{cool})$ and $N_{\mathrm{H}}(\mathrm{MC})$ arise artificially as the result of a local χ^2 minimum.

We therefore assumed the north and south regions have the same absorption and tied together $N_{\mathrm{H}}(\mathrm{MC})$. We also tied together the temperatures $kT(\mathrm{MC}_{cool})$, $kT(\mathrm{MC}_{hot})$ and $kT(\mathrm{HC})$, based on their similarity in the unconstrained fits. The best-fit model (Figure 6, Table 2) is once again not acceptable above 90% confidence, and the residuals are similar to these in the individual fits. A broad residual hump is visible around 0.65−0.80 keV, where emission from the Fe-L shell complex is strong. The hump is not reduced using a multi-temperature model (c6pvmkl) in xspec. This may mean that the plasma is not in collisional equilibrium, or that the emission line code does not reproduce the Fe L-shell line complex. On the other hand, the model does not reproduce the argon and sulfur lines around 2−3 keV, confirming that the HC has multiple components (see §5). Both spectra have marginal peaks with equivalent width of ~50−60 eV at 6.4 keV, which might arise from fluorescence of cold iron.

Although the best-fit models are not formally acceptable, they seem to reproduce the global spectral shapes well. The plasma temperatures, ~0.2 and ~0.6 keV in the MC and ~5.5 keV in the HC, are similar to the results of the individual fits. The $E.M.(\mathrm{MC}_{cool})$ and $E.M.(\mathrm{MC}_{hot})$ have the same ratio in the north and south spectra, confirming that the two spectra are quite similar between 0.3 and 2 keV. The average fluxes of the north and south

spectra are 7 and 9.5 $\times 10^{-14}$ ergs cm^{-2} s^{-1} arcmin^{-2} between 0.5–2 keV and 3.5 and 3.8 $\times 10^{-14}$ ergs cm^{-2} s^{-1} arcmin^{-2} between 2–8 keV, respectively. The 0.5–2 keV band flux is consistent with the unabsorbed flux estimated from the least contaminated *Chandra* spectrum, assuming $N_{\rm H}$ =3$\times 10^{21}$ cm^{-2} (Evans et al. 2003). This result ensures that the *Suzaku* spectra between 0.3–2 keV represent diffuse emission from the Carina Nebula.

The south region has a factor of 2 higher Si abundance and a factor of 4 higher iron abundance than the north region. Abundances of magnesium and nickel may also be enhanced by a factor of $\sim$1.5 and 7–8 in the south, though these lines are situated among the iron L-shell lines and their abundance measurements are strongly affected by the remaining uncertainty in fitting the iron line complex. No other elements show a significant abundance difference.

The derived $N_{\rm H}$ ($\sim 1.8 \times 10^{21}$ cm^{-2}) is consistent with $N_{\rm H}$ to some objects around the Carina Nebula (Seward et al. 1979; Savage et al. 1977). However, Leutenegger, Kahn and Ramsay (2003) argued that these measurements are problematic and suggested a factor of 1.5 higher $N_{\rm H}$ ($\sim 3 \times 10^{21}$ cm^{-2}). When we fixed $N_{\rm H}$ at 3×10^{21} cm^{-2} in the spectral fit, the abundances of silicon, sulfur and carbon, which have emission lines in the low energy slope, significantly increase (see Table 2). This means that abundances of these elements strongly couple with $N_{\rm H}$, and are therefore less reliable.

Since some emission lines such as Mg XI and Fe XVII have residuals on the low energy side, we also tried a non-equilibrium ionization (NEI) model (Table 2). However, the large ionization time scale $\tau \sim 1.7 \times 10^{12}$ s cm^{-3} in the best-fit rather suggests the ionization equilibrium plasma, and therefore the best-fit model did not reproduce the residuals. We also tried multi-temperature models for the cool component, but the result did not improve, either.

7. Discussion

Based on the morphology of the X-ray emission, the X-ray luminosity ($\sim 10^{35}$ ergs s^{-1}) and the plasma temperature ($\sim$0.8 keV), Seward & Chlebowski (1982) argued that diffuse X-ray emission from the Carina Nebula is probably produced by strong stellar winds from early stars colliding with ambient gas. Our results using *Suzaku* and *XMM-Newton* are basically consistent with these previous results, except for a slightly lower temperature ($\sim$0.2, 0.6 keV). The inferred temperature is also similar to the temperature of the diffuse emission of the Omega and Rosette Nebulae, for which Townsley et al. (2003) suggested a stellar wind origin.

What is new in this result is the detailed line diagnostics in the soft energy band, especially below $\sim$1 keV. The study reveals that nitrogen is significantly depleted relative to other heavy elements throughout the observed regions, while the abundance of iron and silicon in the southern portion of the nebula is 2-4 times higher than in the northern portion. Any successful explanation of the diffuse emission from the Carina Nebula must account for these abundance anomalies. In the paragraphs below, we explore possible mechanisms.

The evolved stars in the field, η Car and WR 25, have strong winds rich in nitrogen and

poor in oxygen, resulting from the CNO hydrogen burning process (Davidson et al. 1982; van der Hucht et al. 1981). Strong nitrogen and negligible oxygen lines are observed from the diffuse X-ray plasma immediately surrounding η Car ; the abundance ratio was restricted to N/O >9 (Tsuboi et al. 1998; Leutenegger et al. 2003). Although less evolved massive O stars in general show a nitrogen overabundance, the O stars in the Carina region have a relatively low N/O ratio (Morrell et al. 2005). Even so, the *Suzaku* spectra of the Carina Nebula show no significant nitrogen emission, but show clear oxygen emission lines. The N/O abundance ratio inferred from the spectral fits is $\lesssim$0.4, over 20 times less than around η Car. The abundance distribution is totally contrary to that expected from massive stellar winds, unless the winds somehow heat the interstellar matter without enriching it, thus leaving the X-ray plasma with abundances typical of interstellar matter. At the same time, X-ray luminosity of the Carina Nebula is about two orders of magnitude higher than that of other Galactic star forming regions, but the number of early O stars is only an order of magnitude higher (see Table 4 in Townsley et al. 2003). These results suggest an additional energy source is needed to power the X-ray emission in the Carina Nebula.

An obvious possibility is one or more core-collapse supernovae (i.e. Type Ib,c or II), mentioned as a possibility by Townsley et al. (2003). The north and south regions vary strongly in silicon and iron abundances and marginally in magnesium and nickel abundances. These elements are products of core-collapse supernovae. Moreover, young SNRs such as Cas A and Vela show strong abundance variation from location to location (e.g., Katsuda & Tsunemi 2006).

A single supernova could power the entire Carina Nebula. Assuming a uniform temperature throughout the entire extent of the nebula (1.°1 E-W by 0.°7 N-S (Seward & Chlebowski 1982) by a comparable line-of-sight depth) the total energy content in the hot gas of $\sim 2\times10^{50}$ ergs, a modest fraction of the $\sim 10^{51}$ ergs of kinetic energy produced by a canonical supernova.

On the other hand, the total iron mass in the diffuse gas cannot be the product of a single supernova. Assuming an iron abundance of 0.30 solar throughout the entire nebula implies a total iron mass $M_{Fe} \sim 0.1/n\ M_{\odot}$, where n is the plasma number density in the unit of cm^{-3}. Our results suggest $n \sim 0.2-0.4$ cm^{-3} in the north and south regions. If these regions are representative of the entire nebula then $M_{Fe} \sim 0.25-0.4\ M_{\odot}$. The typical core collapse supernova yields $\leq 0.1\ M_{\odot}$, so more at least 3-5 supernovae would be required to supply the iron.

There is no evidence for supernova remnants in the Carina Nebula in the radio (Whiteoak 1994) or the X-ray. There are two known pulsars, 1E 1048.1-5937 and PSR J1052−5954, within 1° from η Car, but they are located far behind the Carina Nebula (Kramer et al. 2003; Gavriil & Kaspi 2004; Gaensler et al. 2005). Core collapse supernovae produce a wide variety of stellar remnants, however, and not all of them pulse. It is plausible that several stellar remnants similar to those in Cas A and Puppis A (with $L_{\rm X} \sim 2\times10^{33}$ ergs s^{-1} and $kT \sim 5\times10^{6}$ K) could

reside undetected in the Carina Nebula. There is no requirement that the stellar remnants are located within the north or south regions for which we carefully inspected the point sources, or even in the Carina Nebula after $\sim 10^6$ yr.

The need for multiple supernovae to explain the abundances while the energy demands are modest is consistent with a hypothesis advanced by Yonekura et al. (2005) to account for the fact that the strong turbulence in the η Car giant molecular cloud (GMC) observed in CO lines is too energetic to be produced by stellar winds or a single SNR. They suggest that the turbulence was preexisting when the GMC was formed. They postulate that it was produced by the large number of supernovae (>20) responsible for creating the Carina flare supershell (Fukui et al. 1999), and is now dissipating. This suggests that the absence of evidence of SNRs in the Carina Nebula is not a problem, as the explosions that power the X-ray nebula (and the molecular cloud turbulence) occurred $\sim 10^6$ years ago.

The abundance variation between the north and south regions could be one vestige of the multiple explosions. Alternatively, since silicon, iron and magnesium are refractory elements required for silicate grains and can be very strongly depleted from the gas phase in the ISM (Salpeter 1977; Mathis 1996; Draine 2003), we may consider the dust formation or destruction, both of which are strongly associated with the environment of evolved massive stars, to explain the abundance variation.

SNRs thus seem to be a promising hypothesis for explaining the diffuse plasma from the Carina Nebula. However, there are several issues yet to be addressed to confirm this hypothesis. (i). The absolute abundances of all the heavy elements are smaller than solar, unlike in a canonical supernova remnant. Other *Suzaku* observations of diffuse plasma, including the Cygnus Loop supernova remnant (Miyata et al. 1998), also show similar low absolute elemental abundances. This could be simply due to a problem of the current X-ray measurement, such as the need to include a non-thermal continuum component, unknown physical processes of line emission in a very low density plasma, or helium-rich plasma. (ii). The oxygen abundance is relatively low though it should be the most abundant element in core collapse supernova ejecta. In particular, the O/Fe ratio is smaller than the solar ratio.

What is the excess below the O VII line in the north spectrum? Since the other emission lines did not show such an apparent broadening, poor energy calibration is an unlikely cause. The excess can be reproduced by a narrow Gaussian line with a center energy of 0.547 ± 0.01 keV. The error range includes three emission lines from S XIV (10→1, 11→1) and Ca XVI (95→8). However, sulfur and calcium should have stronger peaks below $\lesssim 0.5$ keV when $kT \sim 0.1-0.8$ keV, which are not seen in the spectrum. Though strong radiation from Tr 14 cluster and η Car could photo-ionize the plasma, the excess peak is slightly lower than the forbidden line of O VII at 0.561 keV, which is strong in the photo-ionized plasma (Porquet & Dubau 2000). If the excess is produced by the Doppler shift of the helium-like oxygen line, the velocity is extremely high ($\sim 7.5 \times 10^3$ km s^{-1}). We have no good explanation for this feature.

We should note that a similar excess below O VII is seen from a few *Suzaku* observations such as the North Polar Spur (Miller et al. in preparation).

Less than half of the flux from the hard component arises from known contaminants: X-ray point sources, the CXB and the GRXE. One possible origin of the remainder is a large number of low mass young stars embedded in the cloud, which are too faint to be detected individually. Both the north and south regions include massive clouds (Yonekura et al. 2005), which probably have the star forming activity. Low mass pre-main-sequence stars in the Orion Nebula emit X-rays of kT~0.5–3 keV and L_X $\sim 10^{28.9}$ ergs s^{-1} between 2–8 keV (Feigelson et al. 2005). Since 2–8 keV flux from the Carina Nebula is 2.3×10^{31} ergs s^{-1} arcmin^{-2}, the surface number density of young stars should be $\sim$290 arcmin^{-2} = 650 pc^{-2} at 2.3 kpc. Since the star formation would occur over a parsec scale along the line of sight, the number density should be <650 pc^{-3}, which is small compared with the Orion Nebula (peak of $>10^4$ pc^{-3}, Hillenbrand 1997). There are two problems: hard X-ray flux is almost the same in the two regions even though there are more potential star formation sites in the north; and kT ~5.5 keV is higher than the typical temperature of low mass young stars. Another possibility is that the hard X-ray emission comes from diffuse plasma. Such a very high temperature plasma perhaps needs young supernova remnants (e.g., Koyama et al. 2006), though the observed soft X-ray emission rather suggests presence of old supernova remnants.

8. Summary

We analyzed diffuse X-ray emission from the Carina Nebula using the CCD camera XIS onboard the *Suzaku* observatory. The XIS has the best soft band spectral resolution for extended sources of any X-ray observatory, and provides detailed line profiles and reliable elemental abundances of the plasma. To understand spatial distribution of the diffuse emission, we first analyzed an *XMM-Newton* MOS image centered at η Car. An X-ray color map indicates that the diffuse emission north of η Car is softer than the emission to the south. Analysis of the *Suzaku* spectra shows that this difference arises from a difference in the iron L-shell line intensity. *Suzaku* spectra are roughly divided into three X-ray components. Spectra below ~0.3 keV have almost the same flux in the north and south regions. This component originates in the foreground, including the LHB. The spectra above 2 keV also have almost the same flux and shape. About half of the emission arises from the CXB, GRXE and X-ray point sources detected with *Chandra*. The remainder of the hard emission may be from unresolved pre-main-sequence stars. The spectra between 0.3 and 2 keV are dominated by emission from soft diffuse emission. The spectra show K-shell lines of silicon, magnesium, neon, oxygen, and possibly carbon ions, and L-shell lines of iron ions. The strength of the Si and Fe lines is different between the north and south regions, while the other parts of the spectra are similar. The spectra from both regions are reproduced with a 2T plasma model with kT ~0.2 and 0.6 keV and sub-solar elemental abundances and common absorption of $\sim 2\times10^{21}$ cm^{-2}, but are not

acceptable at the 90% confidence level. A nitrogen line is detected from neither of the spectra, restricting N/O $\lesssim$0.4. Such a low nitrogen abundance is not expected from stellar winds from evolved massive stars, and suggests that the plasma originates from an old SNR, or a super shell produced by multiple SNRs. The south region has a factor of 2−4 higher elemental abundances in iron and silicon than the north region. Magnesium and nickel may show spatial abundance variation, as well. The abundance variation may be explained by the presence of SNR ejecta. Alternatively, dust formed around the star forming core may play an important role.

The spatial structure and abundance variation of the plasma provide clues to the origin of the diffuse emission. For this purpose, a mapping of the Carina Nebula with *Suzaku* and *XMM-Newton* will be important. The spectra are complicated with many emission lines; high resolution spectroscopy on the future satellites, such as an X-ray calorimeter, will be needed to solve the origin of this mysterious X-ray nebula.

K. H. is financially supported by the *Chandra* US grant. M. T. and Y. E. are financially supported by the Japan Society for the Promotion of Science.

References

Albacete Colombo, J. F., Méndez, M., & Morrell, N. I. 2003, MNRAS, 346, 704
Davidson, K., Walborn, N. R., & Gull, T. R. 1982, ApJL, 254, L47
Dickey, J. M., & Lockman, F. J. 1990, ARA&A, 28, 215
Draine, B. T. 2003, ARA&A, 41, 241
Dwarkadas, V. V. 2005, ApJ, 630, 892
Ebisawa, K., et al. 2005, ApJ, 635, 214
Evans, N. R., Schlegel, E. M., Waldron, W. L., Seward, F. D., Krauss, M. I., Nichols, J., & Wolk, S. J. 2004, ApJ, 612, 1065
Evans, N. R., Seward, F. D., Krauss, M. I., Isobe, T., Nichols, J., Schlegel, E. M., & Wolk, S. J. 2003, ApJ, 589, 509
Ezoe, Y., Kokubun, M., Makishima, K., Sekimoto, Y., & Matsuzaki, K. 2006, ApJ, 638, 860
Feigelson, E. D., et al. 2005, ApJS, 160, 379
Fukui, Y., Onishi, T., Abe, R., Kawamura, A., Tachihara, K., Yamaguchi, R., Mizuno, A., & Ogawa, H. 1999, PASJ, 51, 751
Gaensler, B. M., McClure-Griffiths, N. M., Oey, M. S., Haverkorn, M., Dickey, J. M., & Green, A. J. 2005, ApJL, 620, L95
Gavriil, F. P., & Kaspi, V. M. 2004, ApJL, 609, L67
Hillenbrand, L. A. 1997, AJ, 113, 1733
Jansen, F., et al. 2001, A&A, 365, L1
Katsuda, S., & Tsunemi, H. 2006, ApJ, 642, 917
Kelly, R., et al. 2006, PASJ, submitted
Kokubun, M., et al. 2006, PASJ, submitted

Koyama, K., et al. 2006a, PASJ, submitted
Koyama, K., et al. 2006b, PASJ, submitted
Kramer, M., et al. 2003, MNRAS, 342, 1299
Kuntz, K. D., Snowden, S. L., Pence, W. D., & Mukai, K. 2003, ApJ, 588, 264
Leutenegger, M. A., Kahn, S. M., & Ramsay, G. 2003, ApJ, 585, 1015
Mathis, J. S. 1996, ApJ, 472, 643
Mitsuda, K., et al. 2006, PASJ, submitted
Miyaji, T., Ishisaki, Y., Ogasaka, Y., Ueda, Y., Freyberg, M. J., Hasinger, G., & Tanaka, Y. 1998, A&A, 334, L13
Miyata, E., Katsuda, S., Tsunemi, H., Hughes, J. P., Kokubun, M., Porter, F. S. 2006, PASJ, submitted
Morrell, N. I., Walborn, N. R., & Arias, J. I. 2005, PASP, 117, 699
Morrison, R., & McCammon, D. 1983, ApJ, 270, 119
Porquet, D., & Dubau, J. 2000, A&AS, 143, 495
Raymond, J. C., & Smith, B. W. 1977, ApJS, 35, 419
Salpeter, E. E. 1977, ARA&A, 15, 267
Savage, B. D., Bohlin, R. C., Drake, J. F., & Budich, W. 1977, ApJ, 216, 291
Serlemitsos, P. J. et al. 2006, PASJ, submitted
Seward, F. D., & Chlebowski, T. 1982, ApJ, 256, 530
Seward, F. D., Forman, W. R., Giacconi, R., Griffiths, R. E., Harnden, F. R. J., Jones, C., & Pye, J. P. 1979, ApJL, 234, L55
Snowden, S. L., Egger, R., Finkbeiner, D. P., Freyberg, M. J., & Plucinsky, P. P. 1998, ApJ, 493, 715
Strickland, D. K., Heckman, T. M., Colbert, E. J. M., Hoopes, C. G., & Weaver, K. A. 2004, ApJS, 151, 193
Takahashi, T. et al. 2006, PASJ, submitted
Townsley, L. K., Broos, P. S., Feigelson, E. D., & Garmire, G. P. 2005, in IAU Symposium, 227, ed. R. Cesaroni, M. Felli, E. Churchwell, & M. Walmsley, 297–302
Townsley, L. K., Feigelson, E. D., Montmerle, T., Broos, P. S., Chu, Y.-H., & Garmire, G. P. 2003, ApJ, 593, 874
Tsuboi, Y., Koyama, K., Murakami, H., Hayashi, M., Skinner, S., & Ueno, S. 1998, ApJ, 503, 894
van der Hucht, K. A., Conti, P. S., Lundstrom, I., & Stenholm, B. 1981, Space Science Reviews, 28, 227
Weisskopf, M. C., Brinkman, B., Canizares, C., Garmire, G., Murray, S., & Van Speybroeck, L. P. 2002, PASP, 114, 1
Whiteoak, J. B. Z. 1994, ApJ, 429, 225
Wolk, S. J., Bourke, T. L., Smith, R. K., Spitzbart, B., & Alves, J. 2002, ApJL, 580, L161
Yonekura, Y., Asayama, S., Kimura, K., Ogawa, H., Kanai, Y., Yamaguchi, N., Barnes, P. J., & Fukui, Y. 2005, ApJ, 634, 476

Table 1. Best-fit Models of Chandra Point Source Spectra

Parameters		North	South
kT_{cool}	(keV)	0.35	0.14
log $E.M._{cool}$*	(cm^{-3})	56.5	58.4
kT_{hot}	(keV)	4.1	2.5
log $E.M._{hot}$*	(cm^{-3})	55.6	55.7
Abundance	(solar)	0.05	0.007
Gaussian†			
Center	(keV)	0.98	
Normalization	(10^{-6} photons cm^{-2} s^{-1})	9.3	
N_H	(10^{21} cm^{-2})	3.1	6.1
Flux‡	(10^{-13} ergs cm^{-2} s^{-1})	8.4	5.4
$\Delta\chi^2$/d.o.f (d.o.f)		1.59 (40)	1.53 (29)

* Assuming d =2.3 kpc.

† Assuming a narrow Gaussian (σ = 0.0 keV).

‡ Observed X-ray flux between 0.5–10 keV.

Table 2. Spectral Fitting Results

Model		Individual		$N_{\rm H}$(MC), kT tied		$N_{\rm H}$(MC) fixed		NEI		Typical Error*
		North	South	North	South	North	South	North	South	
Medium Component (MC)										
kT_{cool}	(keV)	0.20	0.23	0.21		0.19		0.21		0.01
kT_{hot}	(keV)	0.60	0.58	0.58		0.56		0.57		0.01
log $E.M._{cool}$†	($\rm cm^{-3}arcmin^{-2}$)	56.0	55.0	55.7	55.6	56.2	56.0	55.5	55.3	0.1
log $E.M._{hot}$†	($\rm cm^{-3}arcmin^{-2}$)	55.0	54.9	55.1	55.0	55.0	54.8	55.1	55.0	0.1
$N_{\rm H}$	(10^{21} $\rm cm^{-2}$)	2.4	1.2	1.8		3.0 (fix)		1.8		0.2
C	(solar)	2.5e-2	0.0	0.0	0.0	0.34	0.85	0.0	0.25	5e-2
N	(solar)	0.0	1.2e-2	0.0	0.0	0.0	0.0	1.5e-2	4.5e-2	1e-2
O	(solar)	4.3e-2	0.12	6.2e-2	6.3e-2	4.2e-2	6.1e-2	9.1e-2	0.12	1e-2
Ne	(solar)	8.9e-2	0.14	0.13	9.0e-2	8.1e-2	0.11	0.19	0.14	3e-2
Mg	(solar)	0.11	0.19	0.11	0.16	9.4e-2	0.17	0.11	0.16	2e-2
Al	(solar)	0.17	0.0	7.5e-2	2.9e-2	0.17	0.18			0.2
Si	(solar)	0.10	0.25	9.2e-2	0.24	0.11	0.36	0.11	0.27	2e-2
S	(solar)	0.38	0.12	0.24	0.39	0.48	0.85	0.22	0.43	0.1
Ar	(solar)	0.36	0.0	0.0	0.13	1.4e-2	1.2	1.4e-2	1.2	0.2
Ca	(solar)	0.0	0.0	0.0	0.0	0.0	0.0	0.0	0.0	3e-2
Fe	(solar)	8.4e-2	0.30	7.8e-2	0.30	8.3e-2	0.43	8.3e-2	0.30	1e-2
Ni	(solar)	0.34	0.56	8.9e-2	0.78	0.56	1.9	1.5e-2	0.39	0.1
τ	($\rm s\ cm^{-3}$)							1.7e12		$>$ 9e11
Hard Component (HC)										
kT	(keV)	5.5	5.5	5.3		5.5		5.1		0.2
log $E.M.$†	($\rm cm^{-3}arcmin^{-2}$)	54.4	54.5	54.4	54.5	54.4	54.5	54.5	54.5	0.1
$N_{\rm H}$	(10^{22} $\rm cm^{-2}$)	2.3	1.3	2.4	1.5	1.8	1.2	2.5	1.7	1
Z	(solar)	0.48	0.44	0.47	0.43	0.50	0.44	0.46	0.42	5e-2
$\chi^2/d.o.f$		2.07	2.94	2.70		3.52		2.70		
$d.o.f.$		378	344	736		737		737		

*The typical errors show the range within $\Delta\chi^2$ =2.7.

†Assuming d =2.3 kpc.

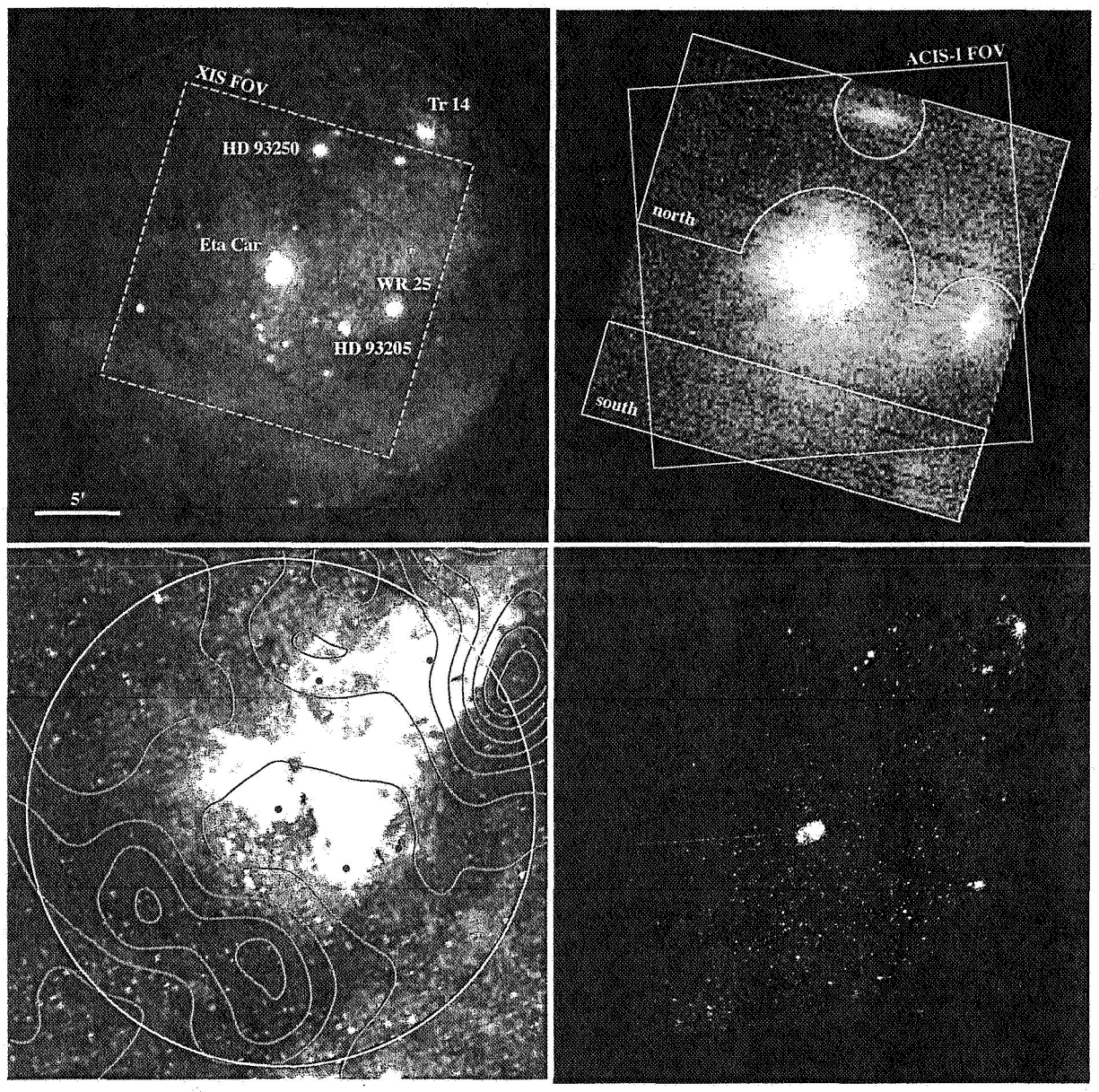

Fig. 1. *Top left*: *XMM-Newton* EPIC MOS image color-coded to represent the soft band (0.2–0.6 keV) to red, medium band (0.6–1.2 keV) to green and hard band (1.2–10 keV) to blue. The bar-dot lines show the XIS FOV in the 2005 Aug. 29 observation. *Top right*: *Suzaku* BI image in the 2005 Aug. 29 observation. The solid white lines show event extraction regions, and the solid green lines show the *Chandra* FOV in the 1999 Sep. 6 observation. *Bottom left*: Integrated intensity map of the ^{12}CO emission (sky blue contour) on the optical image taken from the Digitized Sky Survey (gray scale image), which is a part of Figure 1 in Yonekura et al. (2005). The red spots show the bright X-ray sources introduced in the *top left* image. The yellow circle shows the *XMM-Newton* EPIC MOS FOV. *Bottom right*: *Chandra* image in the 1999 Sep. 6 observation. All the X-ray images are drawn with logarithmic scale and do not correct the vignetting effect.

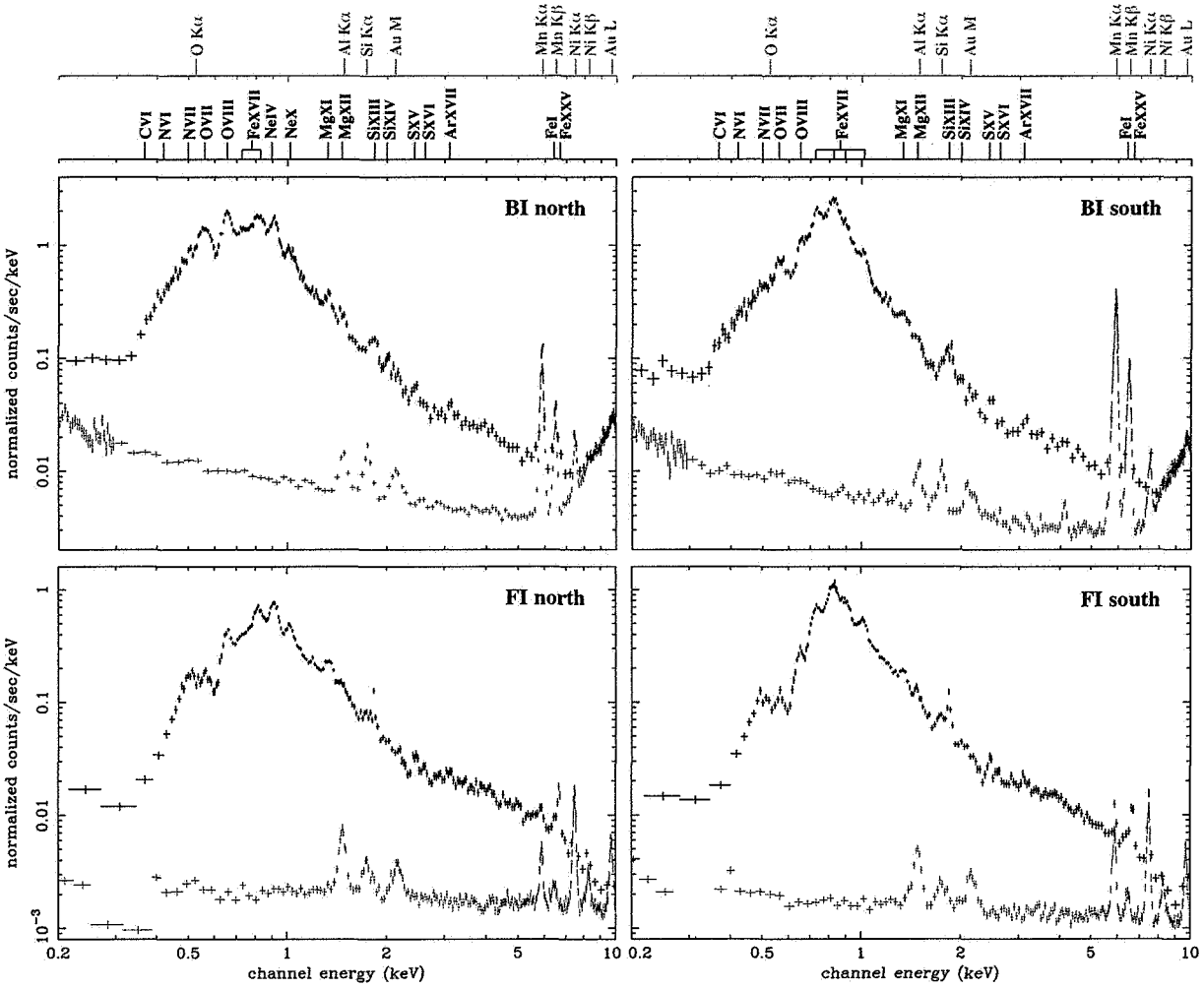

Fig. 2. BI (*top*) and FI (*bottom*) spectra of the north (*left*) and south (*right*) regions. The black shows the source spectra and the grey shows the detector internal background, obtained from night Earth observations. The above labels demonstrate energies of emission lines detected or concerned with this result.

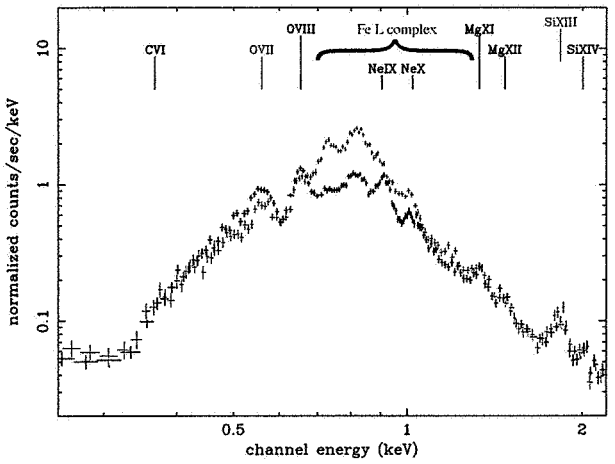

Fig. 3. North (black) and south (red) spectra between 0.3–2 keV overlaid. The north spectrum is normalized by 64%, to adjust the effective area of the south region at 2 keV. The above labels show detected emission lines, among which blue elements exhibit distinct differences between the north and south spectra.

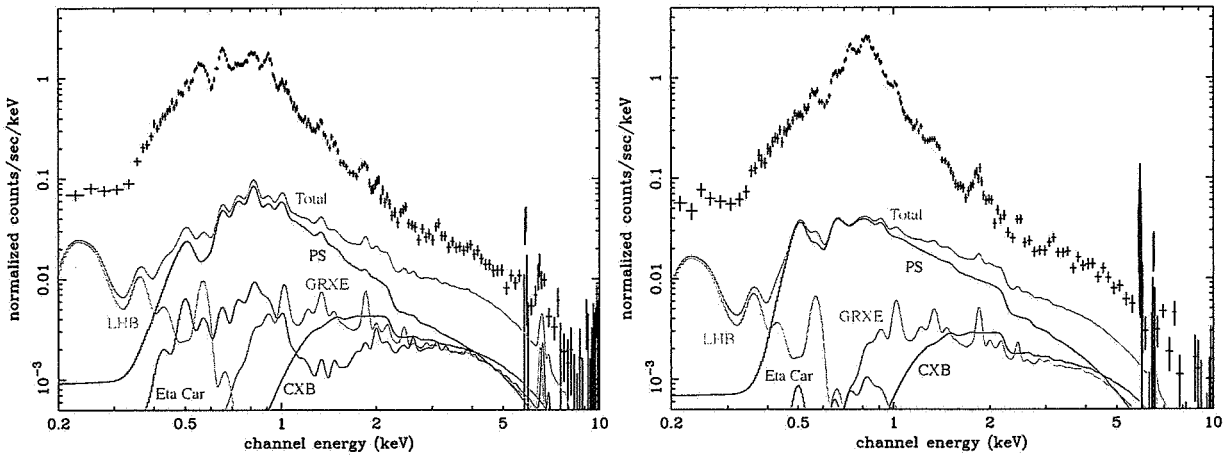

Fig. 4. Background subtracted BI spectra (*left*: north, *right*: south) with possible spectra of contamination sources.

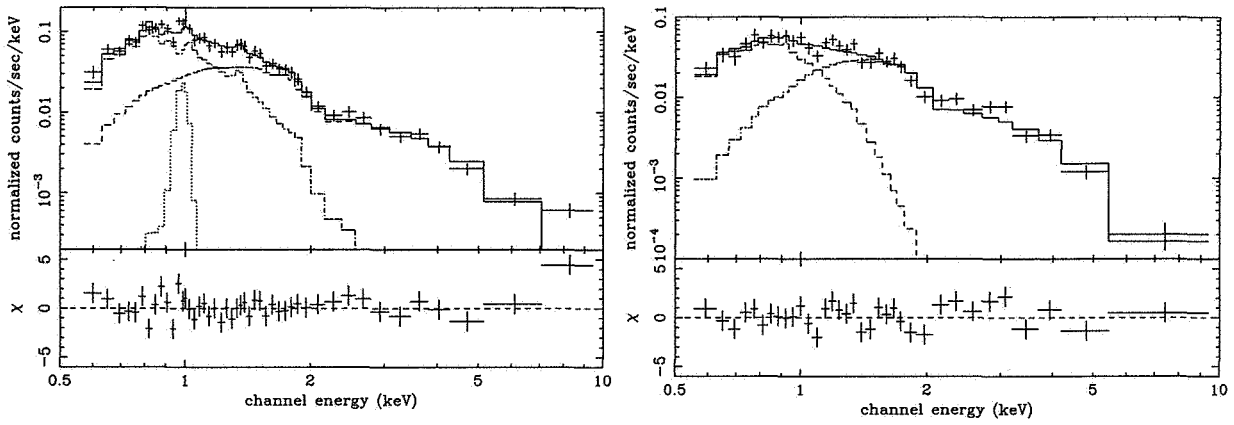

Fig. 5. Combined *Chandra* spectra of point sources in the north (*left*) and south (*right*) regions. Solid lines show the best-fit absorbed 2T models, with a Gaussian for the north spectrum. The bar, dot-bar and dotted lines show each plasma component. The bottom panels show residuals from the best-fit models.

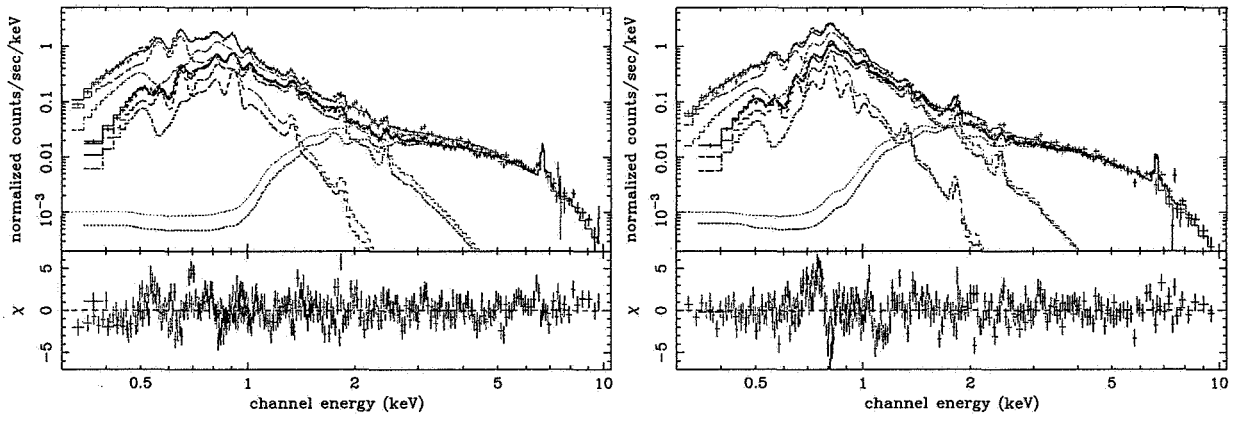

Fig. 6. Best-fit result of the north (*left*) and south (*right*) spectra by the model with $N_{\rm H}$(MC) and kT tied (*black*: FI, *red*: BI). The solid lines and dotted lines show the best-fit model and each of the plasma components, respectively. The bottom panels show residuals in the fits.